ACS APPLIED MATERIALS & INTERFACES

Research Article

www.acsami.org

Electrochromic Behavior of $W_xSi_yO_z$ Thin Films Prepared by Reactive Magnetron Sputtering at Normal and Glancing Angles

Jorge Gil-Rostra,[†] Manuel Cano,[‡] José M. Pedrosa,[‡] Francisco Javier Ferrer,[§] Francisco García-García, Francisco Yubero,[†] and Agustín R. González-Elipe*[,†]

[†]Instituto de Ciencia de Materiales de Sevilla (CSIC-USE), Avenida Américo Vespucio 49, E-41092 Sevilla, Spain

[‡]Departamento de Sistemas Físicos, Químicos y Naturales, Universidad Pablo de Olavide, Ctra. Utrera km. 1, E-41013 Sevilla, Spain

[§]Centro Nacional de Aceleradores (CSIC-USE), Thomas A. Edison 7, E-41092 Sevilla, Spain

Supporting Information

ABSTRACT: This work reports the synthesis at room temperature of transparent and colored $W_xSi_yO_z$ thin films by magnetron sputtering (MS) from a single cathode. The films were characterized by a large set of techniques including X-ray photoelectron spectroscopy (XPS), Rutherford backscattering spectrometry (RBS), Fourier transform infrared (FT-IR), and Raman spectroscopies. Their optical properties were determined by the analysis of the transmission and reflection spectra. It was found that both the relative amount of tungsten in the W−Si MS target and the ratio O_2/Ar in the plasma gas were critical parameters to control the blue coloration of the films. The long-term stability of the color, attributed to the formation of a high concentration of W^{5+} and W^{4+} species, has been related with the formation of W−O−Si bond linkages in an amorphous network. At normal geometry (i.e., substrate surface parallel to the target) the films were rather compact, whereas they were very porous and had less tungsten content when deposited in a glancing angle configuration. In this case, they presented outstanding electrochromic properties characterized by a fast response, a high coloration, a complete reversibility after more than one thousand cycles and a relatively very low refractive index in the bleached state.

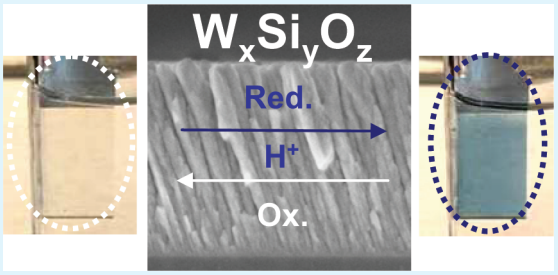

KEYWORDS: *electrochromic films, GLAD, $W_xSi_yO_z$, reactive magnetron sputtering, colored thin films, tungsten oxide, optical properties*

INTRODUCTION

Even if tungsten oxide electrochromic thin films have been studied and manufactured for more than 30 years,[1−4] new developments are still required to improve the behavior of these materials when used for smart windows and other related applications,[5−8] both in the laboratory and at industrial scale.[9] For example, improvements are still required to properly nanostructuring the films to enhance their coloration capacity, to decrease the response time,[10−13] to apply the electrochromic devices on flexible plastic substrates[14−16] or to effectively control their optical properties.[17−19] To cope with all these requirements, new manufacturing processes and novel nanostructures have been proposed to both simplify the film processing protocols and to design more reliable final devices. A commonly admitted requisite in this regard is that the electrochromic films, prepared by sol−gel, electrochemical methods, thermal evaporation, magnetron sputtering or other related procedures,[12,13,20−23] possess a significant portion of empty and accessible space to favor the exchange of charge and the incorporation of foreign cations.

An electrochromic film device based on tungsten oxide consists of a reducible WO_3 layer, another thin film electrode, and an electrolyte where there is a cation M^+ that becomes incorporated in the film during the reduction cycle. Typically, this cation is H^+ or Li^+, although other alkaline cations can be also used.[24,25] For an optimal performance of the device, a fast incorporation of M^+ within the film and its reversible release to the electrolyte during the reduction and oxidation cycles are required, respectively (i.e., $WO_x + e^- + M^+ \rightarrow WO_x(M)$ for the reduction cycle). Optimizing the electrochromic behavior implies to increase the incorporation capacity and to maximize the diffusion rate of the M^+ cation within the film structure.

Compared to sol−gel and other chemical- or solvent-based synthetic routes, MS is a one-step process yielding directly the final formulation of the oxide that has the additional advantage of avoiding the production of undesirable byproducts. The easy scalability of this method and the possibility to work at low temperature open de way for the fabrication of electrochromic films onto polymers. However, a possible drawback of MS thin films is that, because of their generally high compactness, the diffusion rate of M^+ cations are slow and the switching times too long.[26−28] An alternative to the conventional MS

Received: June 6, 2011
Accepted: December 30, 2011
Published: December 30, 2011

processing of WO_x thin films is the use a glancing angle deposition (GLAD) configuration.[29,30] GLAD thin films, prepared by either thermal evaporation or MS are characterized by a columnar microstructure with a high porosity and a pore structure consisting of mesopores extending from the surface of the film up to the interface with the substrate.[31,32] Already in 1995 Granqvist et al.[33] reported about the preparation of WO_3 electrochromic thin films by MS using GLAD. However, even if the open and highly porous character of these films are very promising for their implementation as fast switchable electrochromic layers, to the best of our knowledge, neither a thorough characterization of their electrochromic behavior nor other fabrication essays of WO_x GLAD electrochromic films have been reported in literature.

In the first part of the present work, we present the preparation by MS of $W_xSi_yO_z$ colored thin films for optical applications (e.g., for their implementation as coatings onto colored ophthalmic lenses[34]) where a high transparency in the nonabsorbing spectral regions and well-defined and controllable refraction indices[35] are compulsory requirements. In the second part of the work, we present the fabrication of electrochromic $W_xSi_yO_z$ thin films with a good performance in terms of switching behavior and coloration efficiencies, as well as antireflective properties when they are in the bleached state. For this purpose, we have used a GLAD configuration that yields very porous thin films well-suited to comply with the requisites of electrochromism. Although, mixed oxides thin films of tungsten with other cations have been synthesized with the aim of controlling their optical and gas sensing properties,[17,36,37] only a few works have dealt with their use for electrochromic applications.[37,38] In this regard, it is worth recalling some recent results with $W_xTa_yO_z$ thin films[38] where a fast switching behavior has been related with a distortion of the local arrangement around the W sites because of the presence of nearby Ta atoms. The preparation of $W_xSi_yO_z$ thin films by sol–gel procedures has been also reported in literature.[39]

The present work also reports the characterization by several techniques, and the analysis of the optical properties of a series of $W_xSi_yO_z$ films synthesized by reactive MS under normal and GLAD configurations. It is shown that the color intensity and other optical properties of the films prepared at normal geometry can be tuned by controlling the plasma gas composition and the W/(W+Si) ratio in the films. We have shown that these films depicted a good electrochromic behavior when working in an acid solution (i.e., by using H^+ as exchanged cation), a feature that has been related to their porous nanocolumnar microstructure. Full transparency and antireflective properties (i.e., low refractive index) in the bleached state are two other remarkable properties of this new type of electrochromic materials.

EXPERIMENTAL SECTION

Thin Film Preparation. $W_xSi_yO_z$ thin films have been prepared by reactive pulsed DC MS using a silicon target of 50 mm diameter on which a series of tungsten strips (Goodfellow 99.95%) have been arranged axially as reported in Figure S1 of the Supporting Information. The width of the strips was 1.5 mm. Samples were prepared with 1, 3, and 6 strips along the target diameter. As evidenced by the erosion track formed in the target (a circumference with ~20 mm radius, i.e., 125 mm length), the percentage of sputtered area at the target covered by the tungsten strips was 3.2, 9.5, or 19.1% for the three experimental conditions mentioned above.

The magnetron was operated with a power of 100 W and a pulsed voltage of 400–550 V at a frequency of 80 kHz. The base pressure of the system was 3.0×10^{-6} mbar. The pressure during deposition was fixed at 5.0×10^{-3} mbar. The process gas consisted of O_2/Ar mixtures with mass flow ratios Φ_{O2}/Φ_{Ar} of 0.1, 1.0, and 2.5. The distance between substrate and target was 10 cm. The films were deposited on either silicon, soda lime glass, quartz, or ITO substrates. The samples will be named in the text with the following notation: W*n*-Φ_{O2}/Φ_{Ar}, where *n* is the number of tungsten strips wrapped on the target and Φ_{O2}/Φ_{Ar} refers the mass flow ratio between these two gases in the plasma. Thus, for example, W6–0.1 corresponds to a sample prepared with six tungsten strips wrapped to the Si target and Φ_{O2}/Φ_{Ar} = 0.1. The thin films prepared at GLAD are designated according to the notation W*n*-Φ_{O2}/Φ_{Ar} GLAD.

Thin film growth was carried out at normal geometry, whereby the substrates are parallel to the target or at glancing angle geometry with an angle of 80° between the target and substrate normals.

Thin Film Characterization. Rutherford back scattering spectrometry (RBS) spectra were obtained in a tandem accelerator (CNA, Sevilla, Spain) with a beam of alpha particles with an energy of 1.557 MeV, 1.7 nA of intensity, and ~1 mm diameter. The accumulated doses was 1.5 μC in all cases.

FT-IR spectra were recorded in transmission mode in a Nicolet 510 spectrometer for samples deposited on polished undoped silicon wafers.

Raman spectra were collected in a LabRAM HR High Resolution 800 Confocal Raman Microscope. For the measurements a green laser (He–Ne 532.14 mn), working at 600 line/mm, 100× objective, 20mW, and 0.1 mm pinhole, was used.

X-ray photoelectron spectroscopy (XPS) was used to assess the chemical characteristics of the species at the surface of the samples. XPS spectra were recorded in a ESCALAB 210 spectrometer working in the constant pass energy mode at a value of 20 eV. The binding energy (BE) scale of the spectra was referenced to the C 1s peak of the spurious carbon contaminating the surface of the samples at a value of 284.5 eV. Fitting analysis of the W 4f photoelectron peaks after Shirley background subtraction was carried out with a series of doublet peaks with different binding energies to account for the oxidation and/or coordination states of the W^{n+} cations present in the samples.

UV–vis transmission and reflection spectra were recorded in a Varian Cary 300 apparatus. From these curves, refractive index and extinction coefficient functions of the deposited films were derived by simulating the spectra with a Cauchy formalism[40] to describe the wavelength dispersion of the refractive index and extinction coefficient of the films.

Thin film microstructure of the films deposited on Si (100) wafers (cross-sectional and planar views) was analyzed with scanning electron microscopy (SEM) using a Hitachi S4800 field emission microscope.

Electrochromic Tests. Electrochemical measurements were performed at room temperature in a three-electrode cell equipped with quartz windows. The $W_xSi_yO_z$ thin films deposited on ITO substrates were used as working electrodes. All potentials were measured against and are referred to an Ag/AgCl/KCl (saturated) reference electrode, whereas a Pt foil was used as a counter electrode. Electrochemical measurements were performed with a computer-controlled Autolab PGSTAT30 potentiostat, whereas UV/vis absorbance spectra were recorded on an Ocean Optics high-resolution spectrophotometer. In all experiments, the electrolyte was a N_2 purged 0.1 M $HClO_4$ (Merck p.a.) solution in ultrapure water (Millipore Direct-Q system, >18 MΩ cm). This electrolyte provided the best reproducibility and reversibility of the electrochromic cycles.

RESULTS

1. Composition, Structure, and Chemistry of the $W_xSi_yO_z$ thin films. The RBS spectra of samples W1–0.1, W3–0.1, and W6–0.1 reported in Figure 1 show that the amount of tungsten in the films increases with the number of strips wrapped to the Si target. The experimental and simulated curves, these later calculated by the SIMNRA software,[41] indicate that the distribution of Si and W is homogeneous through the whole sample thickness. The W/(W+Si) atomic

dx.doi.org/10.1021/am2014629 | ACS Appl. Mater. Interfaces 2012, 4, 628–638

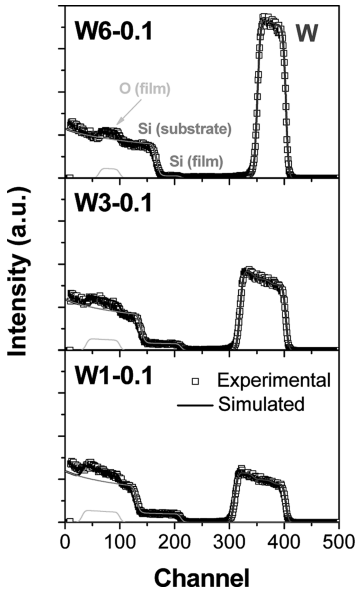

Figure 1. Experimental (square dots) and simulated (continuous gray curves) RBS spectra of $W_xSi_yO_z$ thin films prepared with 1, 3, and 6 strips of tungsten and a Φ_{O2}/Φ_{Ar} ratio of 0.1 (i.e., W1−0.1, W3−0.1, and W6−0.1 thin films).

ratios in Table 1 calculated from the RBS spectra of all samples show a large variation between a value of 0.15 for sample W1−0.1 to 0.77 for sample W6−1.0 (the estimated maximum uncertainty for these calculations is of 5%). These values are similar to those obtained by quantification of XPS spectra, thus confirming that tungsten and silicon atoms distribute homogeneously through the whole thickness of the samples without significant surface segregation effects. Moreover, these data clearly confirm that it is possible to get a precise control of the composition of the $W_xSi_yO_z$ films by using mixed W−Si targets. Although we have tuned this ratio by means of the strip methodology described in the Experimental Section, a similar control is expected with targets made from alloyed mixtures of the two elements.

Table 1. Atomic Percentage Composition and Density of $W_xSi_yO_z$ Thin Films As Determined by RBS and XPS

sample		Si (%)	O (%)	W (%)	W/(W+Si)	density (g/cm^3)
W1−0.1	RBS	21		4	0.15	2.71
	XPS	27	69	4	0.12	
W3−0.1	RBS	17		7	0.28	3.38
	XPS	22	71	7	0.25	
W6−0.1	RBS	6		18	0.74	5.51
	XPS	9	71	20	0.70	
W6−1.0	RBS	5		17	0.77	5.29
	XPS	5	75	20	0.79	
W6−2.5	RBS	5		16	0.76	5.28
	XPS	5	77	18	0.78	
W3−0.1 GLAD	RBS	25		4	0.14	1.95
	XPS	26	70	4	0.13	
W6−0.1 GLAD	RBS	14		13	0.48	2.99
	XPS	14	72	14	0.50	

Even if the small oxygen features have been used for the theoretical simulation of the experimental RBS spectra, no quantitative RBS data on this element are reported in Table 1 because of the large uncertainties derived from the low cross-section of this element. However, the oxygen content estimated by XPS gives a reasonable account of the amount of this element in the films. Thus, by assuming an $xSiO_2 + yWO_3$ composition (x and y are the atomic unit fractions of Si and W reported in Table 1), calculated unit fractions of oxygen of 0.66, 0.65, 0.78, 0.70, and 0.72 are obtained for samples W1−0.1, W3−0.1, W6−0.1, W6−1.0, and W6−2.5, respectively. It must be noted that although the W/(W+Si) fraction of samples W6−1.0 and W6−2.5 was equivalent the latter was fully stoichiometric as deduced from its optical properties and FT-IR analysis described below. These calculated oxygen unit fractions are in relatively good agreement with the experimental values in Table 1, which comparatively show a certain over- (samples W1−0.1, W3−0.1, and W6−1.0) and under-stoichiometry (sample W6−0.1). These differences would be consistent with the surface character of the XPS technique which usually yields an excess of oxygen due to surface adsorption of oxygenated species and with the detection in sample W6−0.1 of W^{5+} and W^{4+} species (see below) whose formation implies a lesser concentration of oxygen in the sample.

Density of the thin films can be also deduced from the mass thickness estimated by RBS and the actual thickness of the films determined from the SEM cross-section images or by optical methods. The calculated density values are reported in Table 1 and plotted in Figure 9. Data for pure SiO_2 and WO_3 prepared under our experimental conditions are also included in the plot. The density for samples W1−0.1 to W6−0.1 increases with the content of tungsten, reaching values similar to the theoretical densities which, ranging between 2.9 and 5.9 g/cm^3, are expected for compact thin films of equivalent compositions.

Although the $W_xSi_yO_z$ thin films were amorphous when examined by X-ray diffraction, some structural information about the films can be obtained by FT-IR and Raman spectroscopies. Figure 2a shows a series of FT-IR spectra corresponding to thin films prepared at normal geometry under different experimental conditions. In comparison with the spectrum of the pure SiO_2 thin film, the spectra of the $W_xSi_yO_z$ samples prepared from targets with 1, 3, and 6 tungsten strips present a progressive decrease in the intensity of the peak at 1070 cm^{-1} attributed to the Si−O−Si vibration in the SiO_2 network.[42] This decrease is not accompanied by an equivalent diminishment of the band at around 950 cm^{-1}, which according to the literature must encompass a contribution from Si−O vibrations[42] and a band due to W═O vibrations.[21,24,42,43] This behavior has to be linked with the increase in tungsten content from sample W1−0.1 to sample W6−1.0 (cf. Table 1). Moreover, the two small features at around 700 and 800 cm^{-1}, which characterize the spectra of these samples, have been attributed in tungsten oxide thin films prepared by various methods[21,24,42−44] to W−O vibrations, where the oxygen−tungsten network presents some distortion.[44] Similar bands have been reported for embedded Keggin structures after their partial reaction with a SiO_2 host matrix.[37]

The Raman spectra of these samples reported in Figure 2b clearly confirm the existence of a structural evolution from samples W1−0.1, W3−0.1, and W6−2.5 to samples W6−0.1 and W6−1.0. In the former set of samples, the peak appearing at 950 cm^{-1}, attributed to the vibration of terminal W═O bonds,[1,15,28,45] and that at approximately 1090 cm^{-1}, due to Si−O−Si vibrations, have a considerable intensity in agreement with the detection in these samples of FT-IR peaks at similar wavelength numbers. The band at 1090 cm^{-1} disappears from

dx.doi.org/10.1021/am2014629 | ACS Appl. Mater. Interfaces 2012, 4, 628−638

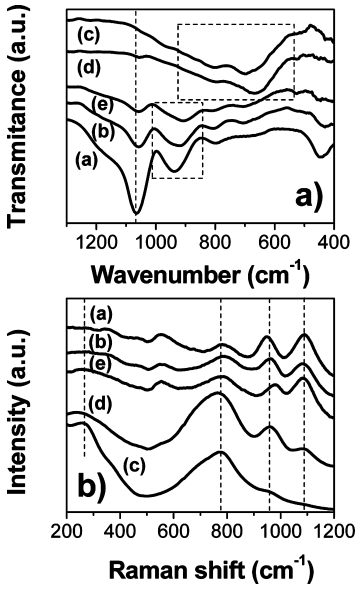

Figure 2. Normalized FT-IR (top) and Raman (bottom) spectra of various $W_xSi_yO_z$ thin films. Curves a, b, and c correspond to thin films prepared with 1, 3, and 6 strips of tungsten and a Φ_{O2}/Φ_{Ar} ratio of 0.1 (i.e., W1−0.1, W3−0.1, and W6−0.1 thin films). Curves d and e correspond to thin films prepared with 6 strips of tungsten and Φ_{O2}/Φ_{Ar} ratios of 1.0 and 2.5 (i.e., W6−1.0 and W6−2.5 thin films). The plotted dashed lines and squares refer to specific bands and groups of bands discussed in the text.

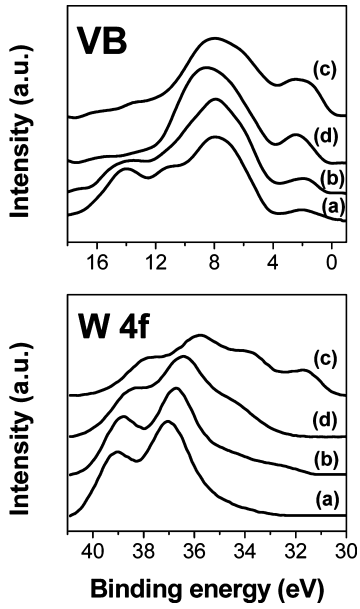

Figure 3. Area normalized VB (top) and W 4f (bottom) photoelectron spectra of $W_xSi_yO_z$ thin films. Curves a, b, and c correspond to thin films prepared with 1, 3, and 6 strips of tungsten and a Φ_{O2}/Φ_{Ar} ratio of 0.1 (i.e., W1−0.1, W3−0.1m and W6−0.1 thin films). Curve d) correspond to a film prepared with 6 strips of tungsten and a Φ_{O2}/Φ_{Ar} ratio of 1.0 (i.e., W6−1.0 thin film). The spectra are vertically displaced for the sake of clarity.

the spectra of samples W6−0.1 and W6−1.0, very likely because in these samples the W−O octahedra constituting the basic structural unit in tungsten trioxide are well interconnected with other W−O octahedral units. The minimum silicon content in these samples seems decisive in favoring an enhanced connectivity of W−O octahedra. The most characteristic feature of samples W6−0.1 and W6−1.0 is the very intense and broad band centered around 780 cm^{-1} that can be attributed to W−O stretching vibrational modes. A similar broad feature has been reported for partially amorphous and/or reduced tungsten oxide,[1,28,45,46] whereas two well-resolved and intense peaks around the same position have been reported for well-crystallized WO_3 thin films.[15,47,48] In sample W6−0.1, the relative intense peak at around 260 cm^{-1} and the shoulder at 330 cm^{-1} can be attributed to W−O−W bending vibrations[15,47] and/or to W−O vibrations associated with W^{5+} species.

The observed tendencies by both FT-IR and Raman spectra can be rationalized by assuming that in samples W1−0.1, W3−0.1, and W6−2.5 there is a $W_xSi_yO_z$ mixed oxide structure where some WO_6 octahedra are not linked by all their corners to other structural units and therefore develop W═O terminal bonds. In samples W6−0.1 and W6−1.0, a better interconnection between the WO_6 and SiO_4 structural units restricts the formation of these terminal bonds. For sample W6−0.1 it has been shown by XPS that there is a certain lack of oxygen in the structure, a feature that agrees with the detection by this technique of W^{6+}, W^{5+}, and W^{4+} species. Tentatively, we assume that the observed reordering and full linkage of the amorphous lattice network can be associated with a high tungsten content and the under-stoichiometry of this sample.

We have advanced that besides varying the number of tungsten strips in the target to get different W/(W+Si) ratios, the control of the Φ_{O2}/Φ_{Ar} ratio in the plasma gas is essential to tune the oxidation state of tungsten in the films. Figure 3 shows the valence band (top) and W 4f (bottom) photoemission spectra of selected $W_xSi_yO_z$ thin films. It is apparent that the centroid of the W 4f photoemission spectra shifts toward lower binding energies with the development of new peaks and/or shoulders when going from sample W1−0.1 to W6−0.1. This shift occurs simultaneously to the development of a new band with a maximum at around 2 eV that edges approximately at the zero of the BE scale of the spectra. This feature is attributed to electronic states localized close to the Fermi level of the tungsten oxide. Its maximum intensity found in sample W6−0.1 is a consequence of the maximum concentration of W^{5+} and W^{4+} states detected in this case. These two parallel results clearly indicate a progressive reduction of the tungsten ions in the $W_xSi_yO_z$ thin films as we increase the number of tungsten strips in the target.[24,49−53] An additional factor that affects the oxidation state of tungsten is the Φ_{O2}/Φ_{Ar} ratio in the plasma gas mixture. This is clearly evidenced by comparing the shape of spectra of sample W6−1.0 with that of sample W6−0.1. In the former, the relatively decrease in the intensity of the feature at the zero of the binding energy scale in the valence band curves and in the lower energy side of the W 4f spectra clearly indicate that sample W6−1.0 is less reduced.[53]

Besides the changes in the W 4f spectra, there are also important modifications in the shape of the O 1s peaks which move from a BE of 532.6 eV for sample W1−0.1 to 531.0 eV for sample W6−0.1 (see the fitted spectra in the Supporting Information, Figure S2). This evolution indicates a transition from a O−Si to a O−W preferential configuration.[53] Additional information about the chemical state of the samples is provided by the analysis of the Si 2p and Si KLL Auger peaks.[54] The Auger parameter, defined as α = binding energy Si 2p + Kinetic energy Si KLL (i.e., as the addition of the BE of the Si 2p photoelectron peak and the kinetic energy of the Si *KLL* main

dx.doi.org/10.1021/am2014629 | *ACS Appl. Mater. Interfaces* 2012, 4, 628−638

Auger transition of the same element) can be related with the polarizability of the matrix.[53,54] When comparing samples W1−0.1 and W6−0.1, changes were observed in both the Si2p BE and the Si Auger KE. These changes render a maximum shift in the Si Auger parameter (i.e., $\Delta\alpha$ for silicon in $W_xSi_yO_z$ and SiO_2) of 2.6 eV for the examined series of samples (an account of this evolution is reported in the Supporting Information, Table S1). This progressive change must be associated with a modification of the local environment around the silicon atom undergoing photoemission.

A deeper insight into the chemical state of tungsten in the prepared samples can be gained by fitting analysis of the W 4f spectra. For the series of studied samples, Figure 4 shows the W

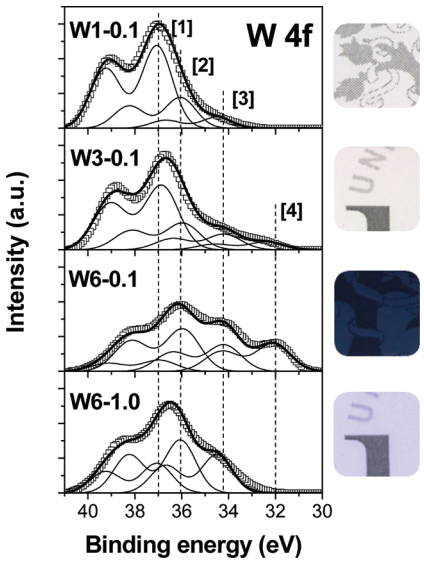

Figure 4. Fitting analysis of the W 4f spectra depicted in Figure 3. [1], [2], [3], [4] and the plotted vertical lines refer to different oxidation and coordination states of tungsten (see Table 2). The insets show images taken for these thin films with a thickness of approximately 300 nm.

4f fitted spectra after background subtraction with a Shirley-type curve. The four spectra can be adjusted with a minimum number of four doublet bands located at 37.0, 36.1, 34.4, and 32.3 eV binding energies for the $W4f_{7/2}$ component. We assume that these bands are due to tungsten ions with different oxidation and coordination states, namely to W_i^{n+} ions in W_i−O−W or W_i−O−Si coordination environments. In previous studies with $M_xSi_yO_z$ thin films formed by the mixture of two oxides with different polarizabilities, we have found that changes in the BE and Auger parameters (i.e., ΔBE and $\Delta\alpha$) of Si and M with respect to the pure oxides of these elements present similar values but have opposite signs.[55,56] This is due to modifications in the Auger parameter of Si and M (in general the Auger parameter of M can also be determined provided that it has a sufficiently intense Auger peak, something which is not the case for W) due to the different polarizabilities of the network in the pure or in the mixed oxide structures. For the same oxidation state, these polarizability effects produce an increase in the BE of ∼1 eV in the M^{n+} cation and a similar decrease in the BE of Si. Therefore, we can assume that for a given W^{n+} oxidation state, its BE will increase by approximately 1 eV if this species is either in a W_i−O−W or a W_i−O−Si configuration. Taking these considerations into account ant the fact that the reduced states of tungsten are more intense in the sample with less silicon (i.e., in samples W6−0.1 and W6−1.0), we attribute the fitting bands in Figure 4 to the following oxidation sates/coordination environments: W_i^{6+}−O−Si, W_i^{6+}−O−W, W_i^{5+}−O− and W_i^{4+}−O−.

Calculation of the area of these components permits to analyze the relative concentration of the different oxidation/coordination states of tungsten in the studied samples. The results of this quantitative evaluation are reported in Table 2,

Table 2. Binding Energies (BE) and Percentage of the Different Oxidation States of Tungsten in the $W_xSi_yO_z$ Thin Films

	[1]W^{6+}−O−Si	[2]W^{6+}−O−W	[3]W^{5+}−O−	[4]W^{4+}−O−
BE (eV)	37.0	36.1	34.4	32.3
W1−0.1	66	25	9	-
W3−0.1	56	23	14	7
W6−0.1	10	39	25	26
W6−1.0	24	44	32	-
W3−0.1 GLAD	69	25	6	-
W6−0.1 GLAD (bleached)	44	45	8	3
W6−0.1 GLAD (colored)	16	44	23	17

showing that in sample W1−0.1, the component W_i^{6+}−O−Si is maximum in agreement with the high concentration of silicon in this sample. This component decreases in intensity for samples W3−0.1 and W6−0.1, where the bands attributed to W_i^{5+}−O− and W_i^{4+}−O− acquire a higher intensity. In sample W6−1.0, the W_i^{4+}−O− component is neglected, indicating a smaller reduction degree in comparison with that of sample W6−0.1.

2. Optical Properties of $W_xSi_yO_z$ Thin Films. An important characteristic of the films prepared with 6 strips of tungsten and a low O_2/Ar ratio was their permanent blue color even after a prolonged (months) exposure of the samples to the air. We attribute this prolonged coloration to the stabilization of the lowest oxidation states of tungsten by the mixed Si−O−W network of these films. From a practical point of view, this result sustains their use as colored coatings for optical and aesthetic applications. Figure 5 shows the UV−vis transmission spectra acquired for the series of studied films with an approximate thickness of 300 nm, together with an image of the films deposited on ophthalmic polymeric substrates. The image and the transmission curves clearly confirm that the W6−0.1 thin films are blue colored and preserve a good transmission in other zones of the spectrum. The blue color is a consequence of the detection of a high concentration of W^{5+} and W^{4+} states. In samples W6−1, W1−0.1, and particularly, W3−0.1, XPS has also revealed the presence of small concentrations of these species. This contrasts with their transparency in the visible (except for sample W6−1, which presented a mild bluish color), a result that we attribute to either a selective reduction of the surface by the X-rays during XPS analysis and/or to the fact that tungsten oxide films with a small concentration of W^{5+} and W^{4+} species may still be transparent.[57]

The color characteristics of the W6−0.1 films can be described by the (*x*,*y*) chromaticity coordinates plotted in the CIE1931 chromaticity diagram presented in Figure 5 (right). The corresponding coordinates (0.27, 0.29) have been evaluated in transmission geometry of the films deposited on

dx.doi.org/10.1021/am2014629 | ACS Appl. Mater. Interfaces 2012, 4, 628−638

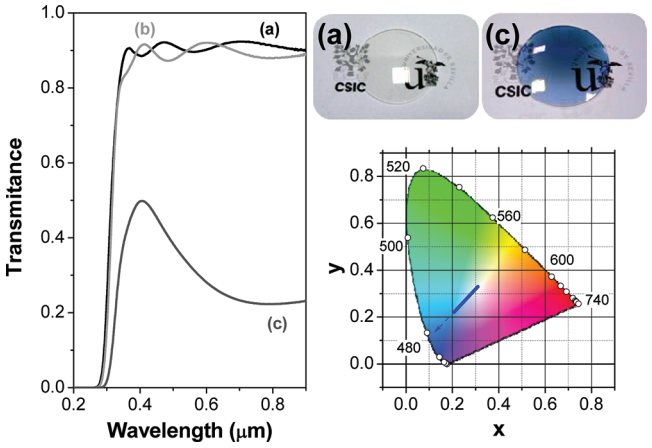

Figure 5. (Left) Transmission spectra of $W_xSi_yO_z$ thin films prepared with 1, 3, and 6 strips of tungsten and a Φ_{O2}/Φ_{Ar} ratio of 0.1, a, b, and c, respectively (i.e., W1−0.1, W3−0.1, and W6−0.1 thin films). (Right-top) Images of the (a) W1−0.1 and (c) W6−0.1 thin films deposited onto polymeric ophthalmic lenses. (Right-bottom) (*x*,*y*) chromaticity coordinates of the W6−01 thin film represented in the CIE 1931 chromaticity diagram as a function of film thickness from 100 to 800 nm.

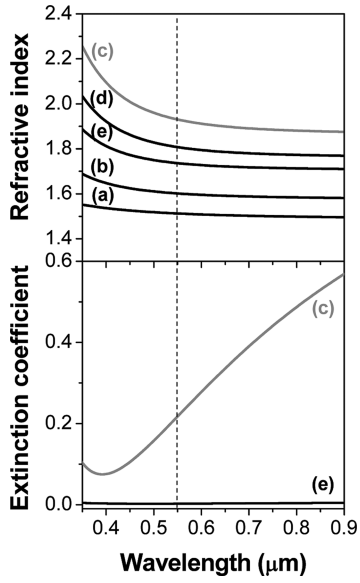

Figure 6. (Top) Refractive index of $W_xSi_yO_z$ thin films prepared by reactive MS and a standard geometry. Curves a, b, and c correspond to thin films prepared with 1, 3, and 6 strips of tungsten and a Φ_{O2}/Φ_{Ar} ratio of 0.1 (i.e., W1−0.1, W3−0.1, and W6−0.1 thin films). Curves d and e correspond to thin films prepared with 6 strips of tungsten and Φ_{O2}/Φ_{Ar} ratios of 0.1 and 2.5 (i.e., W6−0.1, and W6−2.5). (Bottom) Extinction coefficient curves of samples c and e.

soda-lime glass, considering a D65 illuminant, an observer at a second field of view and a thickness of 100 nm. The color coordinates change with thickness according to the direction indicated with an arrow in the diagram. This evolution is due to the broad absorption band starting at about 450−500 nm whose intensity increases at higher wavelengths.

Reflectance spectra for the same series of samples deposited on polished Si(100) are reported in the Supporting Information (Figure S3) together with the results of the fitting analysis carried out to get the refractive index and extinction coefficient as reported in the Experimental Section (see Table S2 in the Supporting Information). The curves plotted in Figure 6 clearly shows that the refractive index *n* of the films increase with the amount of tungsten (i.e., from curves a to c) and with its reduction degree (i.e., from curves d to e), reaching a maximum value of $n = 1.95$ at 550 nm for the W6−0.1 film. The increase in *n* for this sample must be attributed to its relatively high tungsten content and to the high extinction coefficient characteristic of the most reduced films (cf. Figure 6 top). It is worth noting that films prepared with six tungsten strips and having a similar stoichiometry (i.e., $W/(W+Si) \approx 0.75$) in their oxidized state present a lower refractive index together with a very low extinction coefficient (e.g., curve e) in Figure 6 for sample W6−2.5, taken as representative of the noncolored films). A representation of these values as a function of the W/(W+Si) ratio and those for pure SiO_2 and WO_3 prepared under our working conditions is shown in Figure 9. Because of the strict control of the optical properties evidenced in Figure 6 for this kind of film, we have proposed their use as optical coatings for colored ophthalmic lenses.[34]

3. Microstructure, Composition, and Optical Properties of $W_xSi_yO_z$ Thin Films Prepared by GLAD. The thin films discussed so far were prepared at a normal deposition geometry, i.e., with the substrate directly facing the magnetron target. According to the relatively high values of their refractive indices and the density values determined by the SEM/RBS combined analysis (c.f., Table 2), they must present a compact microstructure with no or a little concentration of voids or empty space. This is confirmed by the SEM images of these samples reported in images a and b in Figure 7. Drastic changes in microstructure, composition, and optical properties were

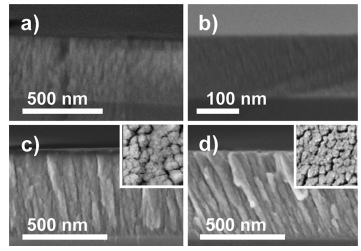

Figure 7. Cross-section SEM micrographs of $W_xSi_yO_z$ thin films prepared with 3 (left) and 6 (right) tungsten strips and a Φ_{O2}/Φ_{Ar} ratio of 0.1. Samples a and b were prepared at normal geometry, whereas samples c and d were prepared at a deposition angle of 80° (GLAD). Inserted micrographs in c and d correspond to the planar view of the same samples.

achieved when the deposition was carried out at glancing angle. Images c and d in Figure 7 show the SEM micrographs corresponding to two $W_xSi_yO_z$ GLAD thin films prepared at a zenithal angle of 80°. These two samples were prepared with 3 and 6 strips of tungsten in the target (i.e., samples W3−0.1 GLAD and W6−0.1 GLAD). According to their cross-section SEM micrographs, these two samples are characterized by a columnar microstructure, where the nanocolumns are separated by large voids and pores as evidenced in the planar view micrographs in this figure (inset images).

Another relevant result in Figure 7 refers to the tilting angle of the columns. Tilted nanocolumns are a characteristic feature of thin films prepared by physical vapor deposition at a glancing geometry.[29−33] A close observation of the cross section micrographs of the two GLAD samples reported in Figure 7 reveals that the tilting angle of the nanocolumns is higher for

dx.doi.org/10.1021/am2014629 | ACS Appl. Mater. Interfaces 2012, 4, 628−638

the film prepared with 6 tungsten strips in the target (i.e., sample W6−0.1 GLAD) than with 3 strips (i.e., W3−0.1 GLAD). Although a thorough analysis of the nanocolumn tilting is outside the scope of this paper, we can advance that the main factor contributing to the observed differences relies on the higher tungsten content in the W6−0.1 GLAD films. During the sputtering deposition, both Si and W atoms are ejected from the target and become randomized by collision with the molecules of the plasma gas (i.e., Ar and O_2) in their trajectory toward the substrate. Because of the momentum conservation law, for a similar average number of collisions, the heavier tungsten atoms will undergo a lesser randomization of their trajectories than the silicon atoms.[57] Under these conditions, shadowing effects and linear trajectories, which are the ultimate factors responsible for the formation of the columnar microstructure,[29−33] are magnified in sample W6−0.1 GLAD because of the preferential deposition of tungsten. As a result, the tilted nanostructure of the W6−0.1 GLAD films approaches the microstructure of thin films prepared by electron evaporation or similar glancing processes in the absence of gas molecules in the evaporation chamber.[58]

Besides these changes in the microstructure, the GLAD thin films presented a significant change in composition when compared with equivalent samples prepared at a normal configuration. The W/(W+Si) ratios in Table 1 determined by XPS and RBS for samples W3−0.1 GLAD and W6−0.1 GLAD clearly evidence that the tungsten content is smaller in these samples than in samples W3−0.1 and W6−0.1. Another significant compositional feature of sample W6−0.1 GLAD was that its oxygen content determined by XPS was 0.72, quite similar to the theoretical value of 0.70 deduced theoretically from the Si and W content in the sample by assuming a full stoichiometry of the constituent oxides. As expected, the "as prepared" W6−0.1 GLAD sample was not colored. Although a thorough description of the causes of this difference with respect to the colored sample W6−0.1 is outside the scope of the present work, qualitatively we can argue that while the amount of less scattered tungsten atoms arriving vertically to the film surface is smaller at GLAD by a cosine factor (the decrease is likely smaller because some scattering of tungsten atoms should actually be occurring), the fully randomized silicon atoms would arrive by a similar proportion at both the glancing and normal configurations. Thus, due to the smaller amount of tungsten in the GLAD films, they result colorless because even for Φ_{O2}/Φ_{Ar} = 0.1, there must be sufficient oxygen in the plasma gas to fully oxidize all tungsten atoms of the films.

These changes in composition for the GLAD samples bring about changes in their structure as determined by FT-IR. Figure 8 shows the spectra recorded for samples W3−0.1 GLAD and W6−0.1 GLAD. As compared with the spectra of samples prepared in a normal configuration (c.f., Figure 3), it is apparent that the shape of the two GLAD samples is similar to that of samples W1−0.1 and W3−0.1, which according to the data in Table 1 present a relatively similar composition. Therefore, similarly to these two latter thin films, we can conclude that in the two examined GLAD samples there is a homogeneous distribution of Si−O tetrahedra and W−O octahedra where some of the WO_6 units are not linked by all their corners and develop W═O terminal bonds.

The open microstructure of the GLAD thin films also produces important changes in their optical properties. The values of n at 550 nm and the density of the GLAD samples

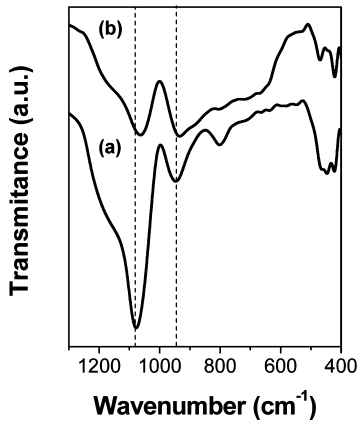

Figure 8. Normalized FT-IR spectra of samples prepared with 3 a) and 6 b) tungsten strips and a Φ_{O2}/Φ_{Ar} ratio of 0.1 at GLAD configuration (i.e., W3−0.1 GLAD and W6−0.1 GLAD).

have been represented in Figure 9 together with values of these two magnitudes determined for the samples prepared at normal

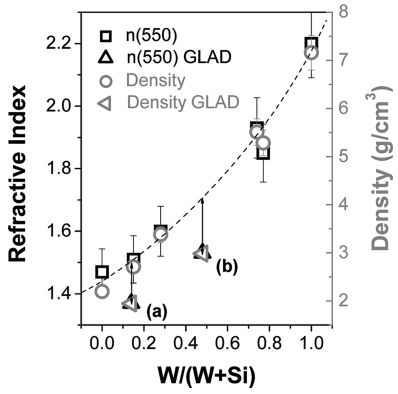

Figure 9. Refractive index and density of $W_xSi_yO_z$ thin films as a function of the W/(W+Si) fraction for films prepared at normal and GLAD geometries. The dashes line are plotted to guide the eyes and to define the range of variation of the plotted parameters for samples prepared by magnetron sputtering in a normal configuration. The signs a and b highlight the points corresponding to samples W3−0.1 GLAD and W6−0.1 GLAD, whereas the vertical arrows show the variation in density and refractive index between a sample prepared under normal configuration to another prepared under GLAD conditions for a similar W/(W+Si) ratio.

geometry. According to this curve, density and refraction indices of the GLAD films drastically decrease with respect to the values of these magnitudes in the films of similar composition prepared at normal geometry. The change in n can be estimated in $\Delta n(550) = -0.15$ and $\Delta n(550) = -0.18$ for samples W3−0.1 GLAD and W6−0.1 GLAD, respectively. The lower density and refractive index of the GLAD samples is directly linked with the development of a porous microstructure with a high content of void space and sustains the use of these films as antireflective coatings when deposited on ITO or even glass.

4. Electrochromic Behavior of $W_xSi_yO_z$ Thin Films. Because of the open and porous microstructure of the $W_xSi_yO_z$ GLAD thin films with the highest tungsten content it is expected a certain electrochromic activity when subjected to voltammetric cycles in the presence of suitable cations. To check this possibility, experiments have been carried out

dx.doi.org/10.1021/am2014629 | ACS Appl. Mater. Interfaces 2012, 4, 628−638

according to the experimental protocol reported in the Experimental Section. Before the description of the corresponding results, it must be advanced that the coloring switching behavior reported below for sample W6−0.1 GLAD was not found for the samples prepared at normal configuration or for sample W3−0.1 GLAD. This suggests that both a highly porosity and a minimum W/(W+Si) ratio are requirements to get a proper electrochromic response.

Figure 10 shows the voltammograms recorded for a fresh W6−0.1 GLAD thin film and for this film activated by cycling

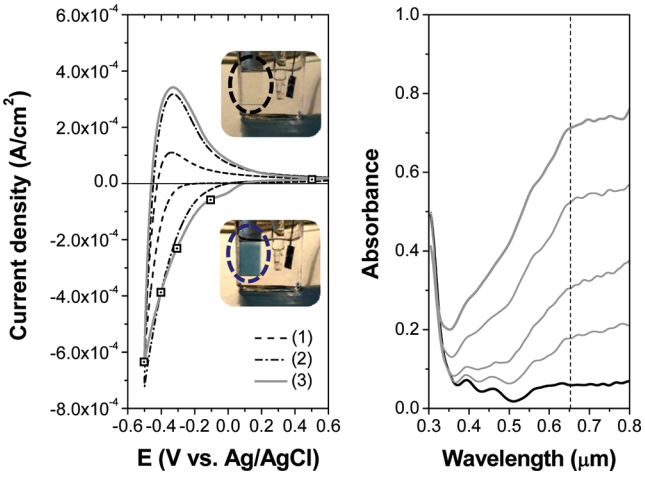

Figure 10. (Left) Successive voltammograms recorded for a virgin $W_xSi_yO_z$ thin film prepared at GLAD with 6 strips of tungsten and a Φ_{O2}/Φ_{Ar} ratio of 0.1 (i.e., thin film W6−0.1 GLAD). Curves 1 to 3 correspond to the three successive cycles required to get steady state conditions (scan rate: 100 mV s^{-1}, working solution: N_2 purged 0.1 M $HClO_4$). The inserted photographs show the film in its bleached and colored states. (Right) Series of UV−vis absorption spectra recorded at different stages of the electrochemical cycle as indicated by the square dotted points in the voltammogram in the left panel of the figure.

the voltage three times up to reach the steady state. Then, the voltammograms were completely reproducible even after more than one thousand cycles (i.e., the curve after this long cycling experiment superimposed perfectly on the curve[3] in Figure 10 (left)). These curves clearly point to a reversible redox process that must be attributed to a change in the oxidation state of tungsten in the films. The attribution of the volta-amperometric curve to a redox process affecting the tungsten in the films is confirmed by the UV−vis absorption curves reported in Figure 10 (right). After the first oxidation run, the sample did not present any significant absorption in the visible but developed an intense absorption after successively cycling the voltage between −0.5 and +0.6 V up to reach the steady state situation. Once reached this state, a reversible change in absorption from a full colored to a bleached state reproduces the reversible cycling of the voltammogram. An outstanding behavior of our films is that the reversible change in color occurs in a reasonably short period of time (i.e., 5 s), being reproducible even after more than one thousand cycles. By eye observation, the color change corresponds to a transformation from transparent to blue, the typical electrochromic behavior reported for other thin films based on tungsten oxides (see for example refs 1, 7, 8, and 14).

Figure 11 reports a series of crono-amperograms cycles and the absorbance of the films at 650 nm, both recorded by

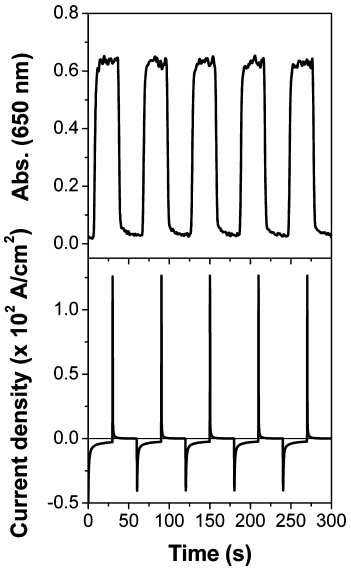

Figure 11. (Top) Evolution of the absorption at 650 nm during five crono-amperogram cycles between +0.8 and −0.6 V to show the reproducibility of the results (bottom).

switching the voltage between +0.8 and −0,6 V. Clearly, these diagrams confirm the complete reversibility of the process. The video provided in the Supporting Information (Video S1) clearly illustrates the good reproducibility and high rate of the color changes. An estimation of the diffusion coefficient of the insertion cation according to the Randles-Servick equation: $i_p = 2.72 \times 10^5 n^{3/2} D^{1/2} C_o \nu^{1/2}$ (where i_p = current density (A/cm^2), n = number of electrons involved in the redox process, D = diffusion coefficient, C_o = cation concentration (mol/cm^3), and ν = scan rate (V/s))[21] yields values between 1.2×10^{-9} and 16.0×10^{-9} cm^2/s for scan rates of 2 and 100 mV s^{-1}, respectively. These values compare well with those calculated for other electrochromic thin films based on WO_3.[21,44,59−61] In the same line, calculation of the coloration efficiency (CE) according to the expression CE = $(\log(T_b/T_c)/q)$ (where T_b and T_c are the transmittances of the film in the bleached and colored states and q = charge density (C/cm^2)) yields a value of 36.65 cm^2/C at a λ = 650 nm, which is comparable with results previously reported for amorphous layers of WO_3.[1,14,16,20,45,62,63]

To ascertain the structural and chemical changes responsible for the color changes and the electrochromic cycling of sample W6−0.1 GLAD, wes analyzed the sample by XPS and by Raman spectroscopy after its removal from the electrochemical bath in the bleached and in the full colored states. The fitted W4f photoelectron spectra in Figure 12 and the percentages of the different oxidation states of tungsten summarized in Table 2 clearly show the formation of a significant amount of W^{5+} and W^{4+} states for this sample in the colored state. It is worth noting that the relative concentration of these oxidation states is similar to that found in the "as prepared" W6−0.1 sample and that this must be the reason for the similarity of their absorption spectra (c.f., compare spectra c of Figure 5 (left) and Figure 10 (right)). On the other hand, the Raman spectrum of the colored sample depicts a very intense peak at around 300 cm^{-1} and a broad Raman band at around 800 cm^{-1}, which in agreement with the spectra of sample W6−0.1 in Figure 2 (bottom) and the related discussion, must be attributed to the partial reduction of the tungsten trioxide. In the bleached state,

dx.doi.org/10.1021/am2014629 | ACS Appl. Mater. Interfaces 2012, 4, 628−638

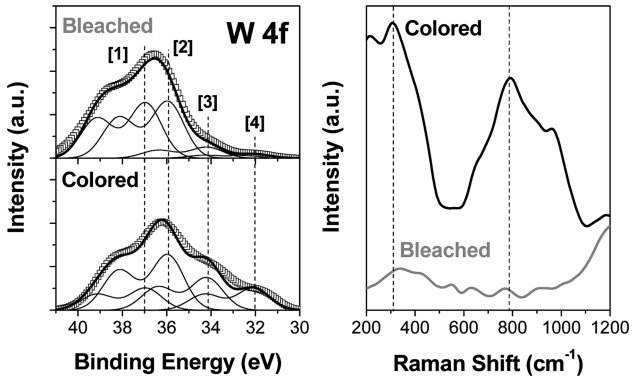

Figure 12. (Left) Fitted W4f photoelectron spectra and (right) Raman spectra of the W6−0.1 GLAD sample taken from the electrochemical bath in the bleached and colored states.

these broad and intense bands disappear from the spectrum further sustaining that they are related with the partial reduction of tungsten ions.

DISCUSSION

Colored Films Prepared by MS. The preparation of nonglazing colored layers to modify the aspect of glass, ceramic, or polymers is an utility with a high potential demand in fields such as the ophthalmic industry, the architectural glass or the decoration of materials.[8,34,35] Most works in the literature dealing with the preparation by MS of semitransparent and colored layers, have tried the incorporation within a dielectric matrix of noble metal nanoparticles (Au, Ag, etc.) characterized by well resolved and intense plasmon structures.[63−65] The approach carried out here consists of preparing a mixed oxide thin film containing a cation (i.e., W^{n+}, $n < 6$) which absorbs the light in the visible region of the electromagnetic spectrum. We have shown that by controlling the number of tungsten strips in the target and the Φ_{O2}/Φ_{Ar} ratio in the plasma gas it is possible to tune both the amount and the oxidation state of tungsten in the film as monitored by RBS and XPS (cf. Figures 1, 3, and 4, Tables 1 and 2). At industrial scale this approach could be improved by using targets of Si−W alloys or mixtures to ensure an automatic reproducibility of results. An outstanding feature of our films is the high stability of the W^{n+} ($n < 6$) states in the samples that when stored for more than 1 year in air presented a colored aspect similar to that after preparation. This is likely associated with the formation of a mixed W−O−Si structure, which besides stabilizing the low oxidation states of tungsten, prevents the diffusion of oxygen and the oxidation of tungsten, at least under normal ambient conditions.

The observed tendencies in composition and oxidation state found in our films can be rationalized by assuming that the sputtered silicon atoms react more easily than tungsten atoms with the oxygen species of the plasma and that, therefore, silicon always appear in the form of Si^{4+} species. In turn, because tungsten is more sensitive to the actual concentration of plasma species of oxygen, this element is partially oxidized when there is a low oxygen concentration in the plasma gas and/or for a high number of tungsten strips in the target (i.e., sample W6−0.1).

From the point of view of the applications in the field of optics or as ophthalmic coatings, the developed procedure provides an independent control of the refractive index and the extinction coefficient of the films. Mixtures of transparent oxides of different refractive indices (e.g., TiO_2−SiO_2,[66,67] Ta_2O_5−SiO_2,[67] WO_3-other oxides,[17,36−38] etc.) have been widely used to control this parameter. Here, we have shown that not only refractive index but also the extinction coefficient can be tuned by mixing appropriate oxide materials in a common structure and by controlling the oxidation state of the constituent cations. Similar conclusions were recently obtained for Si−Cu mixed oxides.[68]

Deposition Angle and Evolution of Optical Properties. Besides the W/(W+Si) ratio in the target and the Φ_{O2}/Φ_{Ar} ratio in the plasma gas, an additional experimental parameter adjusted during the deposition process was the deposition angle. We have found that performing the deposition at glancing angles (i.e., 80°) leads to the formation of a columnar microstructure characterized by tilted nanocolumns forming an angle with the substrate that depends on the W/(W+Si) atom ratio in the film. In contrast with the equivalent samples prepared at normal geometry, the development of this porous microstructure is accompanied by a decrease in the tungsten content and the complete oxidation of this element in the synthesized films. We have already pointed out in the previous section the relationship existing between the tilting angles and the collision events taken place in the plasma phase.[69] Herein, we would also like to stress that the refraction index of the films depends on their microstructure and that the Δn (cf. Figure 9) between the films prepared at normal and glancing geometries is larger the higher the content of tungsten in the films. Within the medium effective approximation the existence of pores and empty space in the films is an important factor leading to variations in their refractive indices.[70] Using the Lorentz−Lorenz model,[70] we have calculated that the percentage of voids in the W3−0.1 GLAD and W6−0.1 GLAD thin films is 25 and 30%, respectively. Despite the crude assumptions implied for the calculation (e.g., we have taken the films prepared at normal geometry as a bulk reference, the pores in the GLAD films can be partially filled with water and the Lorentz−Lorenz approximation might not be necessarily the best for our system) these percentages agree with the expected increase in the porosity of the GLAD thin films when the tilting angles of the nanocolumns increases.[58]

Electrochromic Behavior of $W_xSi_yO_z$ GLAD Thin Films. Because of the high porosity of the $W_xSi_yO_z$ thin films prepared at GLAD configuration, it is expected that they are good candidates for electrochromic applications.[10−13] Such a possibility was already proposed by Granqvist et al.[33] in an early work with GLAD thin films of pure WO_3. To the best of our knowledge, since then, no further work dealing with the use of GLAD thin films for this application has been pursued. Herein, we have demonstrated that the films with the highest porosity and a medium tungsten content (i.e., samples W6−0.1GLAD) perform quite well when used as an electrochromic electrode with H^+ as exchange cation. In fact, these films present values of coloration efficiency (CE) and diffusion coefficient (D), which are equivalent or even better than those of nanostructured amorphous WO_3 films prepared by other methods. Thus, our films were quite stable under the working conditions of the bath, so that the voltammogram and the absorption characteristics in the colored and bleached states remained unmodified even after more than one thousand cycles. This high stability contrasts with the partial degradation found for other amorphous films after so long and repeated cycling experiments.[14] We believe that the incorporation of silicon cations in the oxide network contributes to stabilize of

dx.doi.org/10.1021/am2014629 | ACS Appl. Mater. Interfaces 2012, 4, 628−638

the structure and the W^{n+} ($n < 6$) cations formed electrochemically during the reduction cycle. A similar stabilization effect and an ultrafast electrochromic switching has been recently reported by Schmuki et al.[38] for porous W−Ta mixed oxide thin films, where it has been attributed to a lattice distortion around tungsten because of the presence of tantalum.

The coloration produced in electrochromic WO_3 thin films has been traditionally related to polaron transitions between W^{6+} and W^{5+} cations[16] and, more recently, also between W^{5+} and W^{4+} states.[5,53,71] The XPS analysis of the W6−0.1 and W6−0.1 GLAD films, this latter in the colored state (c.f. Figures 4 and 12 (left)) has shown a high concentration of W^{4+} species in these samples and that the low oxidation states of tungsten are quite stable over time. We have attributed this feature to the formation of a W−O−Si common network. It is likely that such structural stability factor favors the formation of W^{5+} and W^{4+} species during the electrochemical reduction cycle and, therefore, contributes to increase the CE factor of our films.

When describing the electrochromic behavior of the W6−0.1 GLAD films, we showed that they reached a stable final response after their electrochromic activation through three reduction−oxidation cycles. Although further work is still necessary to clarify the effect of this activation protocol, we assume that this initial cycling transforms "in situ" the surface characteristics of the tungsten oxide units into those of a hydrous tungsten oxide. In a previous work by cyclic voltametry of WO_3 and $WO_3{\cdot}H_2O$, Marcel et al.[25] showed that the redox processes, both in the reduction and oxidation sides of the voltammograms, are much more efficient for the latter structure. A similar effect is proposed here to account for the need of a certain activation of our films to get their maximum and reversible redox response.

CONCLUSIONS

In this work, we have shown that it is possible to prepare $W_xSi_yO_z$ mixed oxides thin films at room temperature by reactive magnetron sputtering from a single cathode made of Si and W. Trying to tailor the thin film composition, we have used modified cathodes made of a silicon target with a variable number of attached tungsten strips. A direct correlation exists between the number of W strips in the target and the final W/(W+Si) ratio in the film. By changing this parameter and controlling the O_2/Ar ratio in the plasma gas, we have been able to obtain colored films with a high concentration of W^{5+} and W^{4+} species which are deemed responsible for the observed coloration. The outstanding stability of this color over long periods of time has been attributed to the formation of a common W−O−Si network that would stabilize the lower oxidation states of tungsten. This feature sustains the use of these films for ophthalmic and other optical and aesthetic applications.

When instead preparing the films at a normal configuration (i.e., the substrate sitting parallel to the target), the substrate is placed at a glancing angle with respect to the target, very porous thin films formed by tilted nanocolumns are formed. It has been found that for the same zenithal angle of the substrate, the tilting angle of the nanocolumns depends on the relative amount of tungsten in the films. This feature has been explained by assuming that the tungsten atoms ejected from the target are less randomized by collision scattering with the plasma gas molecules than silicon atoms. Because of the formation of a mixed oxide network together with silicon and to their highly porous character, the GLAD thin films have a much lower refraction index than that of WO_3 thin films and even that of compact $W_xSi_yO_z$ thin films of similar composition.

The porous films with the highest relative concentration of tungsten (i.e., W/(W+Si) = 0.48) present an outstanding electrochromic behavior despite their amorphous character and the relatively low content of tungsten. A coloration efficiency of CE = 36.65 cm^2/C, a diffusion coefficient D ranging between 1.2×10^{-9} and 16×10^{-9} cm^2/s and a complete reversibility after more than one thousand cycles sustain the possibility of incorporating these thin films into electrochromic devices. Although for this application there are more efficient films reported in literature,[21,44,59−61] the stability conferred to the films by the Si−O bond structures and their very low refractive index in the bleached state are remarkable advantages for this application. In addition, the compatibility of MS with flexible substrates makes the synthesized materials good candidates for their integration as electrochromic devices in large areas. However, scaling up the MS process to work in a GLAD configuration would likely require the modification of the conventional set ups with the incorporation of a linear slit displaced with respect to the target normal to ensure that glancing angle conditions are preserved over the whole layer surface.

ASSOCIATED CONTENT

Supporting Information

Si−W mixed target configuration (Figure S1); modifications in the shape of the XPS O1s peaks of $W_xSi_yO_z$ thin film samples (Figure S2); Si Auger parameter of $W_xSi_yO_z$ thin films (Table S1); experimental and simulated reflectance spectra of $W_xSi_yO_z$ thin films prepared on polished Si(100) (Figure S3); fitting analysis to get the refractive and extinction coefficient curves of $W_xSi_yO_z$ thin films and procedure for the evaluation of the refractive index and extinction coefficient of a transparent or weak absorbent thin film (Table S2); video showing in real time the evolution of the color of the sample during several crono-amperogram cycles (Video S1) (PDF). This material is available free of charge via the Internet at http://pubs.acs.org.

AUTHOR INFORMATION

Corresponding Author

*E-mail: arge@icmse.csic.es.

ACKNOWLEDGMENTS

We thank the Junta de Andalucía (Projects P09-CTS- 5189, TEP5283 and FQM-6900) and the Ministry of Science and Innovation (Projects CENIT-ArtDeco, CONSOLIDER CSD2008-00023, MAT2010-21228, and MAT2010-18447) for financial support.

REFERENCES

(1) Granqvist, C. G. *Sol. Energy Mater. Sol. Cells* **2000**, *60*, 201−262.
(2) Granqvist, C. G. *Sol. State Ionics* **1994**, *70/71*, 678−685.
(3) Dautremont Smith, W. C. *Displays* **1982**, *3*, 3−21.
(4) Faughnan, B. W.; Crandall, R. S.; Heyman, H. M. *RCA Rev.* **1975**, *36*, 177.
(5) Zhang, J.; Tu, J. P.; Xia, X. I. N.; Qiao, Y.; Lu, Y. *Sol. Energy Mater. Sol. Cells* **2009**, *93*, 1840−1845.
(6) Shang, H.; White, M. H.; Guarini, K. W.; Solomon, P.; Cartier, E.; McFeely, F. R.; Yurkas, J. J.; Lee, W. C. *Appl. Phys. Lett.* **2001**, *78*, 3139.
(7) Granqvist, C. G. *Adv. Mater.* **2003**, *15*, 1789−1803.

(8) Granqvist, C. G. *Sol. Energy Mater. Sol. Cells* **2007**, *91*, 1529−1598.
(9) Kraft, A.; Rottmann, M. *Sol. Energy Mater. Sol. Cells* **2009**, *93*, 2088−2092.
(10) Wu, W. T.; Liao, W. P.; Chen, J.-S.; Wu, J.-J. *Chem. Phys. Chem.* **2010**, *11*, 3306−3312.
(11) Parka, S. Y; Leeb, J. M.; Noh, Ch.; Son, S. U. *J. Mater. Chem.* **2009**, *19*, 7959−7964.
(12) Wang, J.; Khoo, E.; Lee, P. S.; Ma, J. *J. Phys. Chem. C* **2009**, *113*, 9655−9658.
(13) Brezesinski, T.; Fattakhova-Rohlfing, D.; Sallard, S.; Antonietti, M.; Smarsly, B. M. *Small* **2006**, *10*, 1203−1211.
(14) Gillaspie, D. T.; Tenent, R. C.; Dillon, A. C. *J. Mater. Chem.* **2010**, *20*, 9585−9592.
(15) Hare Krishna, K.; Hussain, O. M.; Julien, C. M. *Appl. Phys. A: Mater. Sci. Process.* **2010**, *99*, 921−929.
(16) Azens, A.; Avendaño, E.; Backholm, J.; Berggren, L.; Gustavsson, G.; Karmhag, R.; Niklasson, G. A.; Roos, A.; Granqvist, C. G. *Mater. Sci. Eng., B* **2005**, *119*, 214−223.
(17) Saygin-Hinczewski, D.; Hinczewski, M.; Sorar, I.; Tepehan, F. Z.; Tepehan, G. G. *Sol. Energy Mater. Sol. Cells* **2008**, *92*, 821−829.
(18) Valyukh, I.; Green, S.; Arwin, H.; Niklasson, G. A.; Wackelgard, E.; Granqvist, C. G. *Sol. Energy Mater. Sol. Cells* **2010**, *94*, 724−732.
(19) González-Borrero, P. P.; Sato, F.; Medina, A. N.; Baesso, M. L.; Bento, A. C.; Baldissera, G.; Persson, C.; Niklasson, G. A.; Granqvist, C. G.; de Silva, F.; Ferreira da Silva, A. *Appl. Phys. Letters* **2010**, *96*, 061909.
(20) Sallard, S.; Brezesinski, T.; Smarsly, B. M. *J. Phys. Chem. C* **2007**, *111*, 7200−7206.
(21) Soliman, H. M. A.; Kashyout, A. B.; El Nouby, M. S.; Abosehly, A. M. *J. Mater. Sci.: Mater. Electron.* **2010**, *21*, 1313−1321.
(22) Patel, K. J.; Panchal, C. J.; Desai, M. S.; Mehta, P. K. *Mater. Chem. Phys.* **2010**, *124*, 884−890.
(23) Washizu, E.; Yamamoto, A.; Abe, Y.; Kawamura, M.; Sasaki, K. *Sol. State Ionics* **2003**, *165*, 175−180.
(24) Deepa, M.; Srivastava, A. K.; Sharma, S. N.; Govind.; Shivaprasad, S. M. *Appl. Surf. Sci.* **2008**, *254*, 2342−2352.
(25) Marcel, C.; Tarascon, J. M. *Solid State Ionics* **2001**, *143*, 89−101.
(26) Liao, C. C.; Chen, F. R.; Kai, J. J. *Sol. Energy Mater. Sol. Cells* **2007**, *91*, 1282−1288.
(27) Deepa, M.; Srivastava, A. K.; Agnihotry, S. A. *Acta Mater.* **2006**, *54*, 4583−4595.
(28) Lin, Y. S.; Wu, S. S.; Tsai, T. H. *Sol. Energy Mater. Sol. Cells* **2010**, *94*, 2283−2291.
(29) Deniz, D.; Lad, R. J. *J. Vac. Sci. Technol.* **2011**, *A 29*, 011020.
(30) Deniz, D.; Frankel, D. J.; Lad, R. J. *Thin Solid Films* **2010**, *518*, 4095−4099.
(31) González-García, L.; Barranco, A.; Muñoz-Páez, A.; González-Elipe, A. R.; García-Gutierrez, M. C.; Hernández, J. J.; Rueda, D. R.; Ezquerra, T. A.; Babonneau, D. *Chem. Phys. Chem.* **2010**, *11*, 2205−2208.
(32) González-García, L.; Lozano, G.; Barranco, A.; Mínguez, H.; González-Elipe, A. R. *J. Mater. Chem.* **2010**, *20*, 6408−6412.
(33) Le Bellac, D.; Azens, A.; Granqvist, C. G. *Appl. Phys. Lett.* **1995**, *66*, 1715−1716.
(34) Fernandez-Serrano, R.; Vilajoana-Mas, A.; Dürsteler-López, J. C.; Gil-Rostra, J.; Yubero-Valencia, F.; González-Elipe, A. R. *Polymer lens comprising a hardening layer, and absorbent layer, and a interferential multilayer and corresponding method*, PCT/ES2010/000100.
(35) Arbab, M.; Finley, J. J. *Int. J. Appl. Glass Sci.* **2010**, *1*, 118−129.
(36) Wang, X.; Sakai, G.; Shimanoe, K.; Miura, N.; Yamazoe, N. *Sens. Actuators, B* **1997**, *45*, 141−146.
(37) Klisch, M. *J. Sol−-Gel Sci. Technol.* **1998**, *12*, 21−33.
(38) Kirchgeorg, R.; Berger, S.; Schmuki, P. *Chem. Commun.* **2011**, *47*, 1000−1002.
(39) Bonnet, J. P.; Onillo, M.; Perrin, J. *Mater. Chem.* **1979**, *4*, 7−16.
(40) Kittel, C. *Introduction to Solid State Physics*, 8 ed., John Wiley & Sons: New York, 2004.
(41) http://max-planck-institut-fuer-plasmaphysik.software.informer.com/
(42) Barranco, A.; Yubero, F.; Cotrino, J.; Espinos, J. P.; Benitez, J.; Rojas, T. C.; Allain, J.; Girardeau, T.; Riviere, J. P.; Gonzalez-Elipe, A. R. *Thin Solid Films* **2001**, *296*, 9−15.
(43) Deepa, M.; Singh, P.; Sharma, S. N.; Agnihotry, S. A. *Sol. Energy Mater. Sol. Cells* **2006**, *90*, 2665−2682.
(44) Ivanova, T.; Gesheva, K. A.; Popkirov, G.; Ganchev, M.; Tzvetkova, E. *Mater. Sci. Eng., B* **2005**, *119*, 232−239.
(45) Lee, S. H.; Cheong, H. M.; Tracy, C. E.; Mascarenhas, A.; Czanderna, A. W.; Deb, S. K. *Appl. Phys. Lett.* **1999**, *75*, 1541−1543.
(46) Balaji, S.; Djaoued, Y.; Albert, A. S.; Ferguson, R. Z.; Brüning, R. *Chem. Mater.* **2009**, *21*, 1381−1389.
(47) Díaz-Reyes, J.; Delgado-Macuil, R. J.; Dorantes-García, V.; Pérez-Benítez, A.; Balderas-López, J. A.; Ariza-Ortega, J. A. *Mater. Sci. Eng. B* **2010**, *174*, 182−186.
(48) Balaji, S.; Djaoued, Y.; Albert, A. S.; Bruning, R.; Beaudoin, N.; Robichaud, J. *J. Mater. Chem.* **2011**, *21*, 3940−3948.
(49) Zhang, J.; Tu, J. P.; Xia, X. H.; Qiao, Y.; Lu, Y. *Sol. Energy Mater. Sol. Cells* **2009**, *93*, 1840−1845.
(50) Charton, P.; Gengembre, L.; Armand, P. *J. Solid State Chem.* **2002**, *168*, 175−183.
(51) Avendaño, E.; Berggren, L.; Niklasson, G. A.; Granqvist, C. G.; Azens, A. *Thin Solid Films* **2006**, *496*, 30−36.
(52) Khyzhun, O. Y.; Solonin, Y. M.; Dobrovolsky, V. D. *J. Alloys Compd.* **2000**, *305*, 1−6.
(53) Leftheriotis, G.; Papaefthimiou, S.; Yianoulis, P.; Siokou, A. *Thin Solid Films* **2001**, *384*, 298−306.
(54) Mejías, J. A.; Jiménez, V. M.; Lassaletta, G.; Fernández, A.; Espinós, J. P.; González-Elipe, A. R. *J. Phys. Chem.* **1996**, *100*, 16255−16262.
(55) Ferrer, J.; Yubero, F.; Mejías, J. A.; García-López, F. J.; González-Elipe, A. R. *J. Appl. Phys.* **2007**, *102*, 084112.
(56) Gracia, F.; Yubero, F.; Holgado, J. P.; Espinós, J. P.; González-Elipe, A. R.; Girardeau, T. *Thin Solid. Films* **2006**, *500*, 19−26.
(57) Berggren, L.; Gunnar, A. L. *Solid State Ionics* **2003**, *165*, 55−58.
(58) Alvarez, R.; Romero-Gomez, P; Gil-Rostra, J.; Cotrino, J.; Yubero, F.; Palmero, A.; Gonzalez-Elipe, A. R. *J. Appl. Phys.* **2010**, *108*, 064316.
(59) Agnihotry, S. A. *Sol. Energy Mater. Sol. Cells* **2006**, *90*, 15−24.
(60) Avellaneda, C. O.; Bulhoes, L. O. S. *Sol. Energy Mater. Sol. Cells* **2006**, *90*, 395−401.
(61) Tsirlina, G. A.; Miecznikowski, K.; Kulesza, P. J.; Borzenko, M. I.; Gavrilov, A. N.; Plyasova, L. M.; Molina, I. Y. *Solid State Ionics* **2005**, *176*, 1681−1686.
(62) Lee, S. H.; Deshpande, R.; Parilla, P. A.; Jones, K. M.; To, B.; Mahan, A. H; Dillon, A. C. *Adv. Mater.* **2006**, *18*, 763−766.
(63) Joraid, A. A. *Curr. Appl. Physics* **2009**, *9*, 73−79.
(64) Sangpour, P.; Akhavan, O.; Moshfegh, A. Z. *Appl. Surf. Sci.* **2007**, *253*, 7438−7442.
(65) Sella, C.; Chenot, S.; Reillon, V.; Berthier, S. *Thin Solid Films* **2009**, *517*, 5848−5854.
(66) Ferrer, F. J.; Frutos, F.; García-López, F. J.; González-Elipe, A. R.; Yubero, F. *Thin Solid Films* **2007**, *516*, 481−485.
(67) Smith, R. C.; Hoilien, N.; Dykstra, C.; Campbell, S. A.; Roberts, J. T.; Gladfelter, W. L. *Chem. Vap. Deposition* **2003**, *9*, 79−86.
(68) Gil-Rostra, J.; Yubero, F.; Fernández, R.; Vilajoana, T.; Artús, P.; Dürsteler, J. C.; Cotrino, J.; Ortega, I.; González-Elipe, A. R. *Opt. Mater. Express* **2011**, *1*, 1100−1112.
(69) Brett, M. J.; Hawkeye, M. M. *Science* **2008**, *319*, 1192−1193.
(70) Aspnes, D. E. *Thin Solid Films* **1982**, *89*, 249−262.
(71) Avendaño, E.; Berggren, L.; Niklasson, G. A.; Granqvist, C. G.; Azens, A. *Thin Solid Films* **2006**, *496*, 30−36.